Application of thiol capped ZnS quantum dots as a fluorescence probe for determination of tetracycline residues

Khawla Mili, Zouhour Hsine, Yves Chevalier, Gilles Ledoux, Rym Mlika

▶ **To cite this version:**

Khawla Mili, Zouhour Hsine, Yves Chevalier, Gilles Ledoux, Rym Mlika. Application of thiol capped ZnS quantum dots as a fluorescence probe for determination of tetracycline residues. Solid State Communications, 2023, 360, pp.115040. 10.1016/j.ssc.2022.115040 . hal-03905050

HAL Id: hal-03905050
https://hal.science/hal-03905050

Submitted on 18 Dec 2022

HAL is a multi-disciplinary open access archive for the deposit and dissemination of scientific research documents, whether they are published or not. The documents may come from teaching and research institutions in France or abroad, or from public or private research centers.

L'archive ouverte pluridisciplinaire **HAL**, est destinée au dépôt et à la diffusion de documents scientifiques de niveau recherche, publiés ou non, émanant des établissements d'enseignement et de recherche français ou étrangers, des laboratoires publics ou privés.

Application of Thiol Capped ZnS Quantum Dots as a Fluorescence Probe for Determination of Tetracycline Residues

Khawla Mili [a,b], Zouhour Hsine [a], Yves Chevalier [b*], Gilles Ledoux [c] Rym Mlika [a*]

[a] Laboratory of Interfaces and Advanced Materials, Faculty of Sciences of Monastir, University of Monastir, 5019 Monastir, Tunisia.

[b] University Claude Bernard Lyon 1, Laboratory of Automatic Control, Chemical and Pharmaceutical Engineering (LAGEPP), UMR CNRS 5007, 69622 Villeurbanne, France.

[c] Université Claude Bernard Lyon 1, Institut Lumière Matière (ILM), UMR CNRS 5306, 69622 Villeurbanne, France.

* Corresponding authors Email: yves.chevalier@univ-lyon1.fr
Mlikarym@yahoo.fr

Abstract.
A new rapid and sensitive fluorescence probe based on zinc sulfide (ZnS) quantum dots (QDs) as a low-cost and environmentally-friendly alternative has been produced for the detection of tetracycline (TCy). ZnS QDs have been innovatively prepared via simple aqueous colloidal method with thioglycolic acid (TGA) as a stabilizer and characterized by infrared spectroscopy, X-ray diffraction, transmission electron microscopy, UV-Visible absorption and photoluminescence spectroscopy. The blue shift of the absorption band and band gap values with respect to that of bulk ZnS materials confirms the quantum confinement effect. IR spectra show the binding of TGA to the surface of ZnS QDs. X-ray diffraction confirms the formation of a cubic phase of ZnS. Temperature-dependent photoluminescence (PL) spectroscopy shows three emission bands at 405 nm, 442 nm and 483 nm ascribed to electronic transitions involving Zn and S vacancies and interstitial sites. TGA-ZnS QDs is able to detect TCy in an aqueous medium with a pH compatible with the pH of biological fluids which highlight the flexibility and applicability of this sensor in real media. Regarding TCy detection by QD fluorescence, a linear relationship of fluorescence intensity and TCy concentration is obtained over the wide range of 25–6000 nM, and the limit of detection (LOD) is as low as 0.03 nM. Thanks to its excellent analytical performance, such ZnS QDs fluorescent probe is a promising sensing platform for the analysis of trace TCy in biological fluids. Current probe was applied for TCy quantification in milk samples with superior results.

Keywords: ZnS, Quantum Dots, Fluorescence quenching, Tetracycline

1. Introduction

Since their first introduction into medicine in the 1940s, antibiotics have been widely used both in human healthcare and livestock farming throughout the world [1–3]. The presence of residual concentrations of these antibiotics in foods and their release in the environment is a significant danger for human health and aquatic life [4]. Tetracycline antibiotics (TCy) are a variety of important broad-spectrum antibiotics [5,6] that is widely used in human medicine and in animal breeding thanks to their excellent antibacterial properties and low cost. In particular, TCy allows keeping livestock in good health and thereby increases feeding efficiency toward faster animal growth [7]. Unfortunately, the overuse of TCy for growth promotion in animal breeding can result in the presence of drug residues in food of animal origin, including milk, meat, honey, fish, eggs and shrimp [8]. Long-term consumption of foods containing TCy residues results in the development of drug-resistant bacteria and generate several diseases in humans [9,10] such as anaphylactic reactions, gastrointestinal disorders and hepatotoxicity [11,12]. Accordingly, many countries have restricted the maximum residue limits (MRLs) of TCy in foods. MRLs are 0.1 mg kg^{-1} for milk, 0.2 mg kg^{-1} for eggs, 0.3 mg kg^{-1} for liver meat, and 0.6 mg kg^{-1} in kidney meat in EU [13]. The US FDA has also established MRLs of 0.4 mg kg^{-1} for milk, 12 mg kg^{-1} for fat, 6 mg kg^{-1} for liver meat, and 2 mg kg^{-1} for muscle meat [14].

Several analysis approaches for quantitative determination of TCy have been developed during the last few decades. Liquid chromatography-mass spectrometry (LC/MS) [15], high performance liquid chromatography (HPLC) [16] and thin-layer chromatography (TLC) [17] are the most common techniques for the detection of TCy. However, implementation of chromatographic methods is time-consuming, requires skilled operators and high-cost equipment. Other methods including capillary electrophoresis (CE) [18], capillary electrophoresis-mass spectrometry (CE-MS) [19] and enzyme-linked immunosorbent assays (ELISA) [20] have shown high sensitivity and accuracy, but there are still some limitations such as the complex sample preparation procedure and the need for a highly qualified technical staff. There is a need for alternative strategies for sensing TCy in a simple, rapid, selective, sensitive and user-friendly manner. Methods based on fluorescence are of high sensitivity and easy operation, they allow a rapid detection and possibly *in situ* analyses [21]. Significant attention has been paid to fluorescence sensors for the detection of TCy [22,23] using various nanomaterials like gold nanoparticles [24], magnetic nanoparticles [25] and quantum dots (QDs) [26].

Fluorescence sensor based on water-dispersed nanomaterials favorably meets the analytical specifications for the detection of TCy [21,27]. Their unique size-dependent features including easy functionalization, tunable absorption and emission spectra, high stability and large fluorescence quantum yields aiming at selective detection make them ideal fluorescent materials for being implemented into chemical and biological assays [28]. Several fluorescent sensors have been used for the detection of TCy, however their major problem is that the detection takes place in acidic or basic medias which limit their real application in biological fluids. As a few examples, Zhang et al. have developed a fluorescent sensor based on silver nanoclusters (Ag NCs) for the detection of TCy at pH = 5 [33]. Guo et al. used copper doped carbon dots (Cu-CDs) as fluorescence probes for detection of TCy at pH = 4 [34]. However, the detection of TCy in an acidic medium may limit the applicability of these sensors in real media.

To the best of our knowledge, there have been no reports of TCy fluorescence detection in a stable biological environment (pH = 7) using thioglycolic acid functionalized Zinc based QDs. The present work addresses the development of a fluorescence probe designed for a rapid detection of low concentrations of TCy in aqueous medium with physiological pH. It is based on zinc sulfide (ZnS) QDs synthesized by a simple aqueous method using thioglycolic acid (TGA) as a stabilizer. In order to optimize the detection characteristics, pH values were also optimized. The results showed that the emission of ZnS QDs showed a strong synchronous fluorescence, a good stability and high selectivity in a neutral medium, indicating that zinc based QDs may be regarded as a suitable choice for detection of TCy in real media.

2. Experimental section

2.1. Reagents and Materials

Zinc acetate di-hydrate ($Zn(CH_3COO)_2.2H_2O$, 98%), sodium sulfide nonahydrate ($Na_2S.9H_2O$, 98%), thioglycolic acid (TGA, $C_2H_4O_2S$, 98%), sodium hydroxide (NaOH, ≥ 97%), and tetracycline ($C_{22}H_{24}N_2O_8$, ≥ 95%) were purchased from Sigma-Aldrich. Deionized water of resistivity 18 MΩ cm has been used as the solvent for all steps of the ZnS QDs synthesis and for fluorescence measurements in aqueous media. All chemicals were used as they were purchased without further purification.

2.2. Instruments

The Fourier transform infrared spectra of ZnS QDs capped with TGA have been measured by a Nicolet Is50 FTIR spectrometer in transmittance mode at room temperature.

X-ray diffraction patterns (XRD) have been recorded at room temperature by an Ital Structures APD 2000 powder diffractometer using the Cu Kα radiation and a 2θ scan rate of 2 °C min^{-1}. The angular resolution was 0.055 °.

The morphology and size of ZnS particles have been determined by means of a JEOL JEM 1220 transmission electron microscope (TEM) operating at 120 kV. The samples were dispersed in water, deposited onto a thin Formvar film supported on a Cu grid, and dried in open air before TEM observation.

The UV–vis spectra of aqueous colloidal dispersions of ZnS particles have been taken using a UV–vis spectrophotometer Shimadzu UV-310PC over a wavelength range of 200−800 nm) at room temperature. Quartz cells of 1 cm optical path were used.

Photoluminescence spectra have been recorded by exciting the samples with a 10 mW CW laser model UF-F-355 (355 nm) from CNI laser focused on a spot of a 2 mm diameter. The sample has been placed on a Linkam stage THMS600 in which the temperature can be varied between 80 and 300 K. The luminescence spectra have been collected thanks to an optical fiber and fed into a Jobin-Yvon TRIAX320 monochromator coupled to a Newton EMCCD from Andor. The resolution of the system was 2 nm for all the performed measurements.

The surface potential changes upon pH variation have been monitored through zeta potential determination by means of electrophoresis measurements using a Zetasizer NanoZS (Malvern, UK) instrument.

Fluorescence experiments have been carried out on a Cary Eclipse fluorescence spectrometer. The spectra were collected in the range of 350−490 nm with an excitation of 325 nm.

2.3. Preparation of TGA-capped ZnS quantum dots

The ZnS QDs have been prepared in the presence of thiol capping agent (TGA) in accordance

with procedures reported in the literature with minor modifications [32,33]. The Zn^{2+}/S^{2-}/TGA molar ratio of 1/0.5/2.5 was used, corresponding to the stoichiometric requirement generating adequate coverage and full saturation of the dangling bonds on the surface of the QDs with the thiol groups. First, 0.1 M of $Zn(Ac)_2$ and 14.3 mmol of TGA were dissolved together in 50 mL of water. The mixture was adjusted at pH 11 by adding 1 M NaOH, and magnetically stirred for 45 min at room temperature under N_2 atmosphere. Thereafter, 25 mL of Na_2S solution (0.1 M) was added for operating the chemical reaction. The resulting QDs solution has been agitated for about 2 h at 100 °C under N_2 atmosphere. The obtained ZnS nanoparticles were precipitated with ethanol, separated by centrifugation at 4000 rpm, and then dried in a desiccator under vacuum.

2.4. Preparation of the TCy solutions and of TGA-ZnS QDs solution

In a typical test, one millimole of TCy has been dissolved in 10 mL deionized water to make a 10^{-1} M stock solution, which was then diluted to the appropriate concentrations and the pH adjusted as needed. All spectroscopic measurements of synthesized QDs were carried out in an aqueous solution containing 20 mg of dry QDs dispersed in 100 mL of water (0.2 mg mL^{-1}) [36]. To investigate the influence of the quenching by TCy on the fluorescence intensity of TGA-ZnS QDs, various concentrations of TCy were added to a 2 mL calibrated test tube, diluted to the mark with deionized water, and well shaken. After equilibration for 5 min at room temperature, the fluorescence spectra were recorded in the wavelength range of 350–480 nm with an excitation wavelength of 325 nm.

3. Results and discussion

3.1. Chemical and structural characterization of synthesized MPA capped ZnS QDs

3.1.1. Fourier transform infrared (FTIR) studies

The IR spectrum of ZnS stabilized by TGA (**Fig. 1**) allowed identification of the coating of the particles by TGA. The peaks for the S–H vibration (2550–2670 cm^{-1}) were absent in TGA capped ZnS QDs. The origin of the disappearance of the S–H group vibration on the surface of ZnS QDs is due to the strong interaction between the electron doublet of sulfur and the zinc atoms on the surface of the QDs. [34,35]. The absorption spectrum of TGA-ZnS given in **Fig. 1** shows an absorption band at 562 cm^{-1} corresponding to Zn–S stretching vibrations [39]. Besides, this spectrum shows the stretching bending corresponding to C–S, C–H and C–O at 784 cm^{-1}, 899 cm^{-1} and 1226 cm^{-1}, respectively [38]. The intense bands at 1375 and 1560 cm^{-1} are assigned to C=O symmetric and asymmetric stretching modes resulting from the absorption of atmospheric CO_2 on the surface of the ZnS QDs [39,40]. The broad band around 3000−3600 cm^{-1} is due to the O–H stretching of water absorbed on the surface of QDs. These results clearly confirm the binding of TGA on the surface of ZnS QDs.

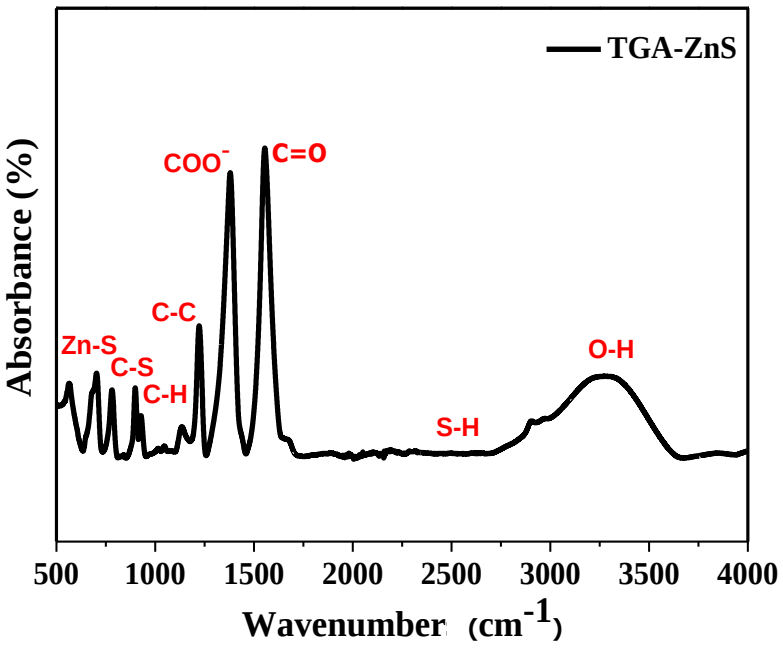

Fig. 1. IR spectrum of TGA-ZnS nanoparticles.

3.1.2. X-ray diffraction (XRD) analysis

XRD gives information about many parameters such as d-spacing, crystal structure, crystal size and even the composition of the material [41]. **Fig. 2** shows the XRD pattern of the synthesized X–ZnS QDs. The three diffraction peaks at 2θ values of 28.6 °, 47.90 ° and 55.27 ° correspond to the (111), (220) and (311) diffraction planes of the crystalline structure of ZnS. The broad diffraction peaks in the XRD pattern show the production of TGA-capped ZnS quantum dots having small crystallites. In addition, no impurity-related reflections were found in the pattern, confirming the high purity of the final product. The comparison with the standard card (JCPDS No. 80-0020) proves the formation of a cubic Zinc Blende structure. The average crystallite size (D) has been calculated from the full width at half maximum (FWHM) measured by fitting the Gaussian profile to the Bragg peaks of the (111), (220) and (311) planes using the Debye-Scherrer equation:

$$D = K\lambda/\beta\cos\theta \qquad (1)$$

where D is the average crystallite size, K is the geometric factor (0.9), λ is the X-ray wavelength (1.54 Å for Cu Kα), β is the FWHM of the diffraction peak (in radian) and θ is the Bragg diffraction angle. The average crystallite size of TGA-ZnS was estimated to be 10.6 nm. The dislocation density (δ) which represents the amount of defects in the sample is determined from the average crystallite size D by using the relationship ($\delta = 1/D^2$) [42]. The d-spacing is calculated using the relation ($d_{hkl} = n\lambda / 2\sin\theta$) [43]. The lattice parameter of TGA-ZnS QDs is a = 5.4 Å. All these structural parameters are listed in **Table 1**.

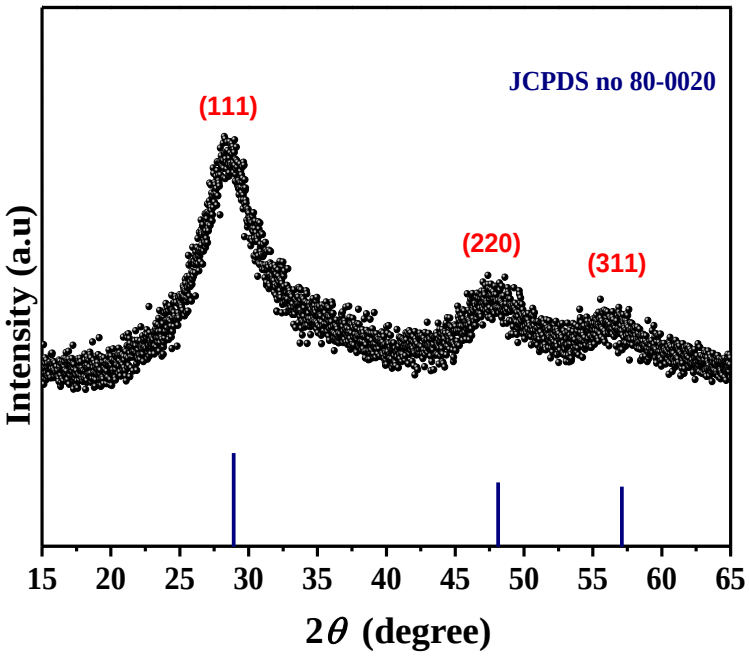

Fig. 2. X-ray diffraction (XRD) pattern of TGA-ZnS nanoparticles.

Table 1. Structural parameters of TGA-ZnS QDs.

2θ (°)	Plane (hkl)	Interplanar spacing d (Å)	Lattice constant a (Å)	Average crystallite size D (nm)	Dislocation density δ (lines/m^2)
28.6	(111)	3.117			
47.9	(220)	1.896	5.4	10.6	8.95×10^{15}
55.27	(311)	1.660			

3.1.3. TEM study

The TEM image in **Fig. 3**(a) indicates the formation of nano-sized crystals with a quasi-spherical shape, which is similar to the results published by several researchers [44–46]. **Fig. 3**(b) shows the particle size distribution resulting from 100 measurements, and the best fit of a Gaussian size distribution to it. The estimated average particle size of TGA-ZnS is 10.63 ± 0.6 nm with a standard deviation of 5.6%. This result is consistent with DRX measurements.

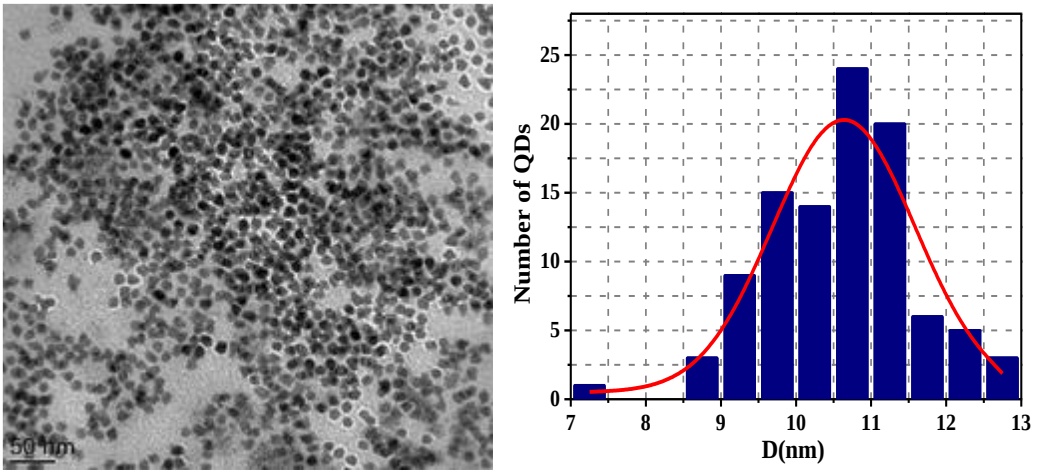

Fig. 3. (a) TEM image of TGA-ZnS QDs. (b) Particle size distribution measured from 100 QDs.

3.2. Photophysical characteristics of the TGA capped ZnS QDs

3.2.1. Band gap determination from optical studies

UV-Visible absorption spectra of the dispersed solution of TGA-capped ZnS QDs (**Fig. 4**(a)) has shown an absorption band at 297 nm which was related to the first electronic transition $1S_e$-$1S_h$ [36]. This is much lower than that of the bulk ZnS crystal (344 nm), that indicated the formation of a smaller crystal with a significantly reduced diameter that is smaller than the excitonic radius of the material. Hence, the information from the absorption spectrometer confirms the formation of QDs.

In order to know the actual value of the band gap, the Tauc diagram is one of the most efficient and famous methods [47]. The values of absorption intensity and energy parameters are allowed to determine the band gap energy (E_g) of ZnS QDs by using the Tauc relation:

$$\boldsymbol{\alpha h\nu = A(h\nu - E_g)^n} \qquad (2)$$

where, α is the absorption coefficient, $h\upsilon$ is the incident photon energy, A is a constant, E_g is the band gap energy of the material and the exponent n is a constant (n = 1/2 for direct semiconductors).

The band gap of TGA-ZnS QDs was determined by a linear extrapolation of $(\alpha h\nu)^2$ to the x-axis (**Fig. 4**b). The band gap was found to be 3.99 eV. There was a blue shift compared to the bang gap of bulk ZnS (E_g = 3.6 eV), which is caused by quantum confinement of charge carriers [48–50].

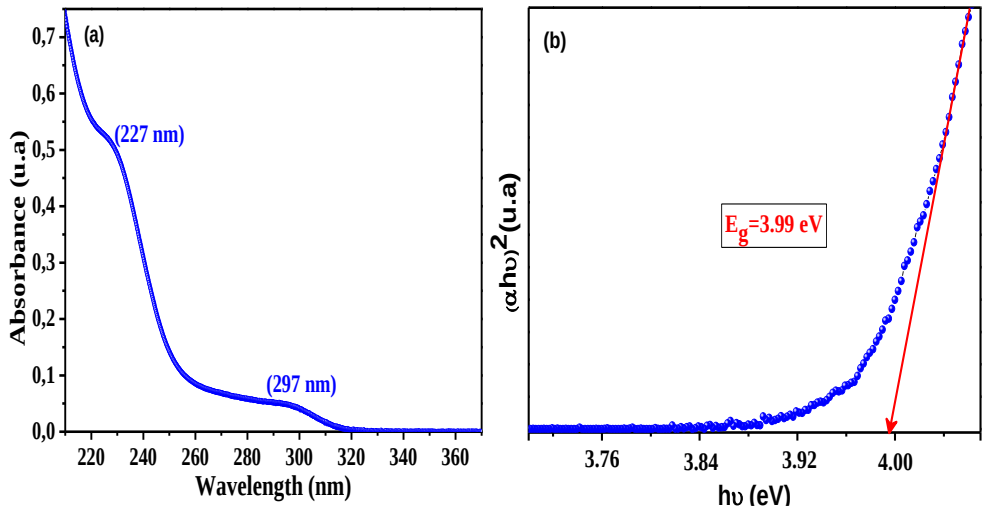

Fig. 4. (a) Absorption spectrum of TGA-ZnS nanoparticles and (b) graphical method for the calculation of their optical gap energy.

3.2.2. Photoluminescence studies

The photoluminescence of ZnS quantum dots is complex, as it is influenced by several synthetic conditions like refluxing time, capping agent and its concentration, reaction temperature, agitation etc. [51,52] and crystal sizes and shapes [53,54]. It is reported in literature that the emission spectrum of ZnS can be adjusted in a very broad range from 300 nm to 550 nm [55]. Typically, two emission peaks can be observed from semiconductor nanoparticles: exciton luminescence and luminescence from trapped electronic states. In most cases of ZnS, a broad blue emission (centered around 400–500 nm) has been reported, which

was ascribed originating from surface defect states [56,57]. However, in this work, as shown in **Fig. 5**(a), for the TGA capped ZnS QDs, there appears an asymmetrical and broadened emission with two distinct maxima. A major peak centered at ~405 nm and a second minor peak at 484 nm are observed, respectively. It is interesting to mention that the broad PL emission of the ZnS QDs is related to the transitions originating from sulfur vacancies [58].

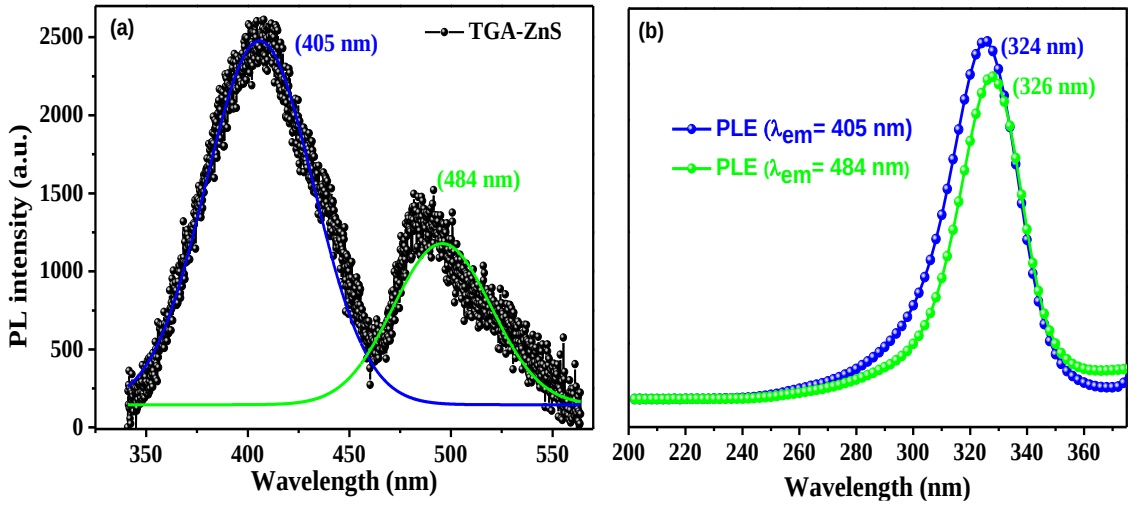

Fig. 5. (a) Gaussian band deconvolution for photoluminescence spectra of TGA-ZnS nanoparticles recorded for λ_{exc} = 325 nm and **(b)** PL excitation spectra recorded for the 405 nm (blue line) and 484 nm (red line) emission bands at room temperature.

The emission peak observed at 405 nm is assigned to the defect trapping states present in the ZnS QDs caused by sulfur vacancies [55,59–61]. During the synthesis, the passivating ligands' thiol group (–SH) is separated from the organic part, which is subsequently attached to Zn ions. These organic groups are responsible for suppressing Zn dangling orbitals. However, the unsaturated sp^3 hybridized orbitals of the surface dangle out of the crystals surface provoking deep hole trap states. This leads to red shifted emission at longer wavelengths, as observed at 484 nm in our case, and also has been reported by others [51,62].

The photoluminescence excitation spectrum (PLE) is a very effective method to study electronic transitions in materials with a high sensitivity compared to absorption measurements [63]. **Fig. 5**(b) also shows a representative PLE spectra of the sample corresponding to the emission at 405 nm and 484 nm, which is centered at ~326 and ~324 nm, respectively. The PLE spectra red-shifted compared to the corresponding absorption spectrum centered at 297 nm. These red-shifted PLE spectra suggest that the lowest electronic levels of the excited states contribute dominantly to the PL emissions.

3.2.3. Temperature dependent PL spectroscopy

Thermal evolution of the photoluminescence (within the range of 80 K ≤ T ≤ 300 K) has been studied, which revealed in details the role of optically active defect states in carrier storage and escape. The PL spectra obtained at various temperatures from 80 K to 300 K of TGA-ZnS powder are plotted in **Fig. 6**. The PL spectrum of these QDs is different at low temperature from the one observed at room temperature. Cooling more clearly reveals the emission from defects in the materials [64]. In addition, a new peak appears at 442 nm arising from the interstitial zinc lattice defects when the temperature decreases [57].

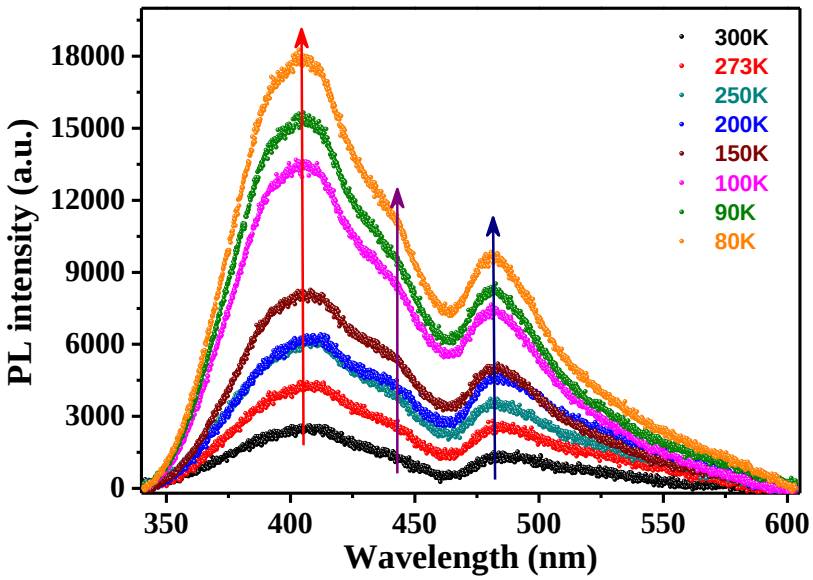

Fig. 6. The temperature-dependent PL spectra of ZnS-TGA nanocrystals.

The PL peak position and intensity as a function of measurement temperature are shown in **Fig. 7**(a,b). At low temperature (80 K), the emission spectra of ZnS QDs contain three large bands located at 405 nm (Peak I), 442 nm (Peak II) and 483 nm (Peak III). The PL bands clearly turned narrower as their intensities have increased (**Fig. 7**b). In fact, the width at half maximum (FWHM) of the defects emission increases with temperature together with a slight change of the position of their maximum (**Fig. 7**a). This temperature dependence of these bands is indicative of a thermal process, which is probably due to the fact that the impurity levels (trap state or surface defects) in the band gap are tightly attached to the ZnS-TGA lattice [65].
The intensities of three trappings, on the other hand, rose at lower temperatures, which was attributable to the elimination of phonon-coupled thermal quenching and differing temperature sensitivity between trapping and exciton states of QDs [66,67].

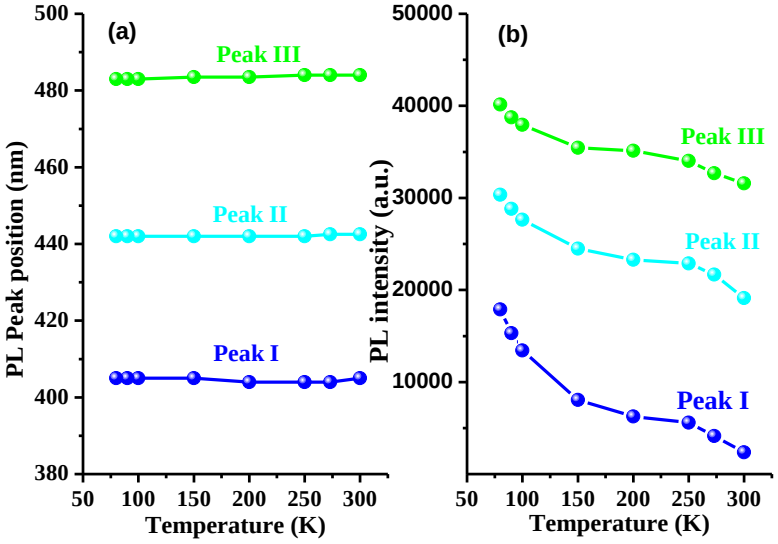

Fig. 7. (a) PL peak position and (b) PL intensity as a function of temperature for Peak I, Peak II and Peak III defects.

The schematic diagram which describes the emission mechanism of the TGA-ZnS QDs is presented in **Fig. 8**, which shows the three-trap state emission in ZnS QDs. In the ZnS QDs, these excited electrons decompose successively in certain defect states such as sulfur vacancy (V_S), interstitial sulfur (I_S) atoms and interstitial zinc (I_{Zn}) atoms by normal recombination. According to a previous work on defects in ZnS QDs, Sulfur atom vacancies (V_S) and zinc atom interstitials (I_{Zn}) are donor states, while interstitials of sulfur atoms (I_S) are acceptor states [59,65].

The introduction of additional zinc and sulfur atoms into the crystal sites can cause the deformation of the host crystal lattice. The atomic size of the incorporated atoms has a significant impact on the amount of deformation. Because sulfur ions are bigger than zinc ones, they will cause more strain in the lattice than zinc ones [68]. It results in a low binding energy value for sulfur interstitial states compared with that for zinc interstitials. The modest binding energy value of interstitial sulfur states minimizes the separation between its energy level and the valence band when compared to the energy difference between zinc interstitial and conduction band [68]. Similarly, the separation of energy between the sulfur vacancy and the conduction band edge is smaller than that between the zinc vacancy and the valence band edge [68]. Additionally, vacancy states are situated at deep energy levels than the interstitial states [65,68]. Taking all these facts into consideration, when comparing the emission of interstitial sulfur states to that of zinc interstitial states, it can be deduced that the emission of interstitial sulfur states arises at a shorter wavelength [68]. Following a molar ratio of Zn/S $\geq$ 2, the synthesized QDs contains an excess of zinc or a sulfur deficiency. Similarly, defect-related emissions were assigned to a transition to the valence band from either an interstitial sulfur atom (I_S), an interstitial zinc atom (I_{Zn}), and a sulfur vacancy (V_S) [69].

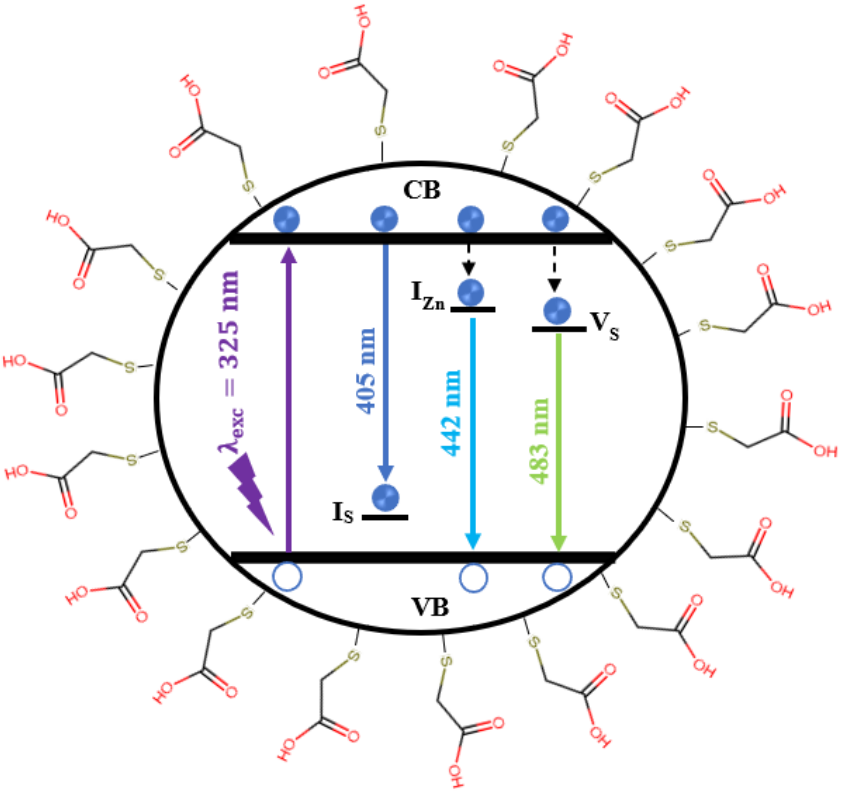

Fig. 8. Transitions leading to PL emission in TGA-ZnS QDs at 80 K; CB- Conduction Band, VB- Valence Band, I_S- Interstitial Sulfur, I_{Zn}- Interstitial Zinc, V_S- Sulfur Vacancy.

3.3. Fluorescence detection of TCy

3.3.1. Effect of pH

The acidity and basicity of the solution plays an important role in the fluorescent properties of TGA-ZnSe QDs. The zeta potential of the TGA-ZnS QDs have been measured in pH range between 1 and 13 to find the most suitable pH condition (**Fig. 9**(a)). The TGA-capped ZnS QDs have negative charges in all the selected pH range. This is explained by the ionization of the carboxylic acid moiety of the TGA, which causes a negative charge on its surface [70]. **Fig. 9**(b) shows the charge of TCy at different pH. Moreover, the higher and lower pH provokes an electrostatic repulsive interaction with the ZnS QDs as recently reported [33]. highly acidic media are not suggested as the TGA-ZnS QDs dissociate via protonation of the surface-bound TGA [71,72] and the interaction between TGA ligand and ZnS QDs can be destroyed, resulting in decreased stability of the QDs [73–75]. In addition, at higher and lower pH, TC may be slightly denatured [76], pH = 7 was selected in this study for the formation of the TGA-ZnS QDs/TCy complex through hydrogen bonding with the neutral zwitterionic form of TCy and the fluorescence quenching detection of TCy. Apart from the good formation of the TGA-ZnS QDs/TCy complex provided by the pH = 7, this pH value is compatible with the pH value of the biological fluids which make our TGA-ZnS sensor easily applied in real media without needing to change its pH.

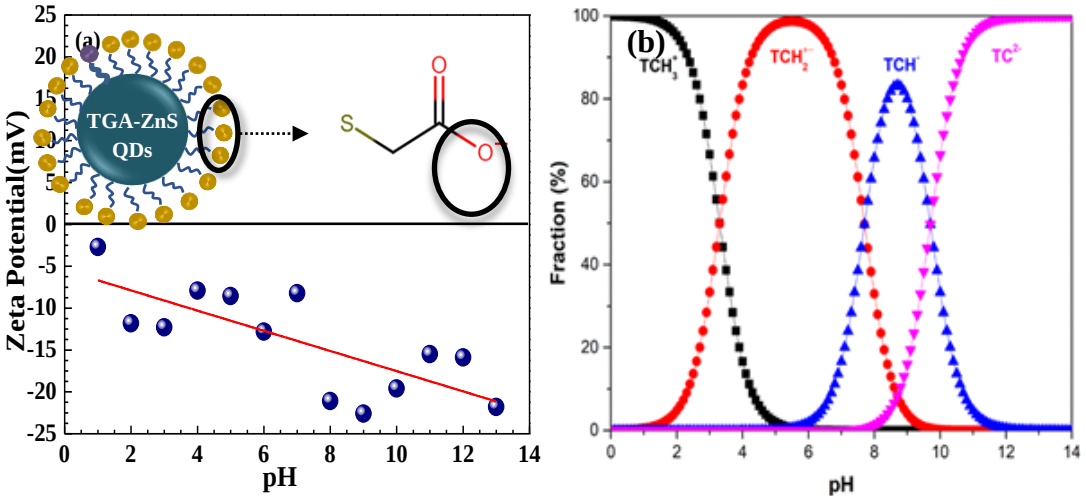

Fig. 9. (a) Zeta potential of the TGA-ZnS QDs at different pH values, (b) pH-dependent speciation of the tetracycline molecule.

3.3.2. Stability of the TGA-ZnS QDs Fluorescence Emission Measurement

The excellent stability of QDs is the prerequisite for their application as fluorescent probes. In order to investigate the stability of fluorescence intensity, fluorescence signals of the TGA-ZnS QDs were recorded every 5 min .As shown in the results in **Fig. 10**(a), the emission of ZnS QDs showed good stability at pH = 7 with a relative standard deviation (RSD) of 0.27%.

3.3.3. Influence of incubation time

The influence of incubation time on the fluorescence intensity was investigated and the result is shown in **Fig. 10**(b). It could be seen that the fluorescent intensity decreases rapidly upon adding TCy. The reaction between TGA-ZnS QDS and TCy was completed within 5 min. After that, the fluorescent intensity remains stable for at least 1 h. Therefore, the ZnS fluorescence spectra in the presence of different concentrations of TCy were recorded after 5 min.

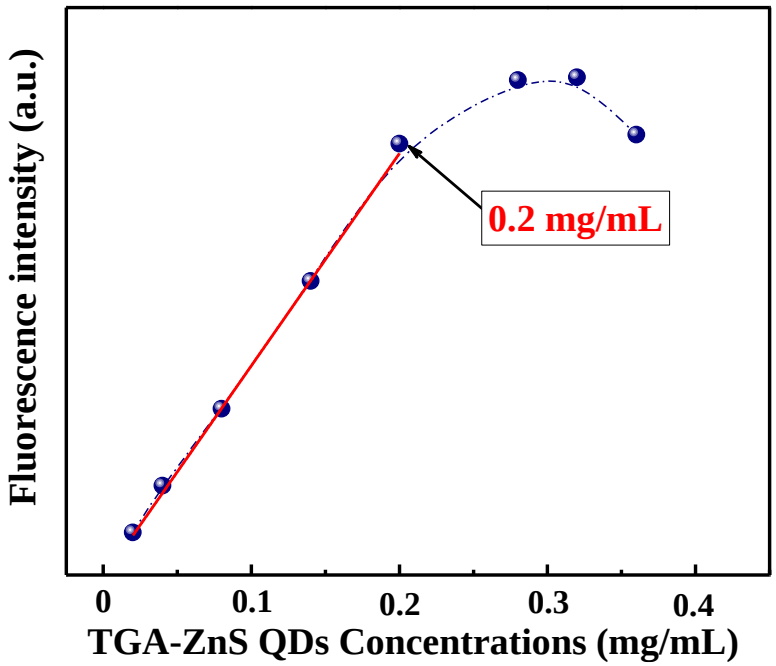

Fig. 10. The fluorescent intensity of TGA-ZnS QDs versus its different concentrations.

3.3.4. Detection of TCy by fluorescence quenching of TGA-ZnS QDs fluorescence

The detection performance was evaluated under the optimal conditions determined above. As depicted in **Fig 11**(a), the fluorescence intensity is decreasing gradually upon increasing the TCy concentration. **Fig. 11**(b) reveals a linear relationship between the inverse fluorescence intensity F_0/F and the concentration of TCy according to the Stern–Volmer equation [77]

$$F_0/F = 1 + K_{SV}\,[\mathrm{TCy}] \qquad \textbf{(3)}$$

where F_0 and F are the fluorescence intensities of the QDs in the absence and the presence of TCy, respectively, K_{SV} is the Stern–Volmer constant, and [TCy] refers to the corresponding concentrations of TCy.

As can be seen, **Fig. 11**(b) shows two linear parts at low and high concentrations of TCy which prove the affinity of the TGA-ZnS towards TCy analytes. Furthermore, as recently reported [33], the downward curvature plot at low concentration (**Fig. 11**(b)) may indicate that dynamic quenching is predominant at low concentration, with a static quenching mechanism at higher concentrations.

The calculated Stern–Volmer quenching constants K_{SV} of TGA-ZnS QDs (which represents the quenching efficiency) from the linearized equation are found to be $K_{SV} = 8.87\times10^5$ L mol^{-1}. This high value of the Stern–Volmer quenching constant demonstrates the excellent quenching efficiency of TCy as well as good affinity of TCy for adsorption to TGA-ZnS QDs. Additionally, the limit of detection (LOD) has been calculated as $3\sigma/K = 0.03$ nM (σ is the standard deviation of the blank, and K is the slope of the calibration curve).

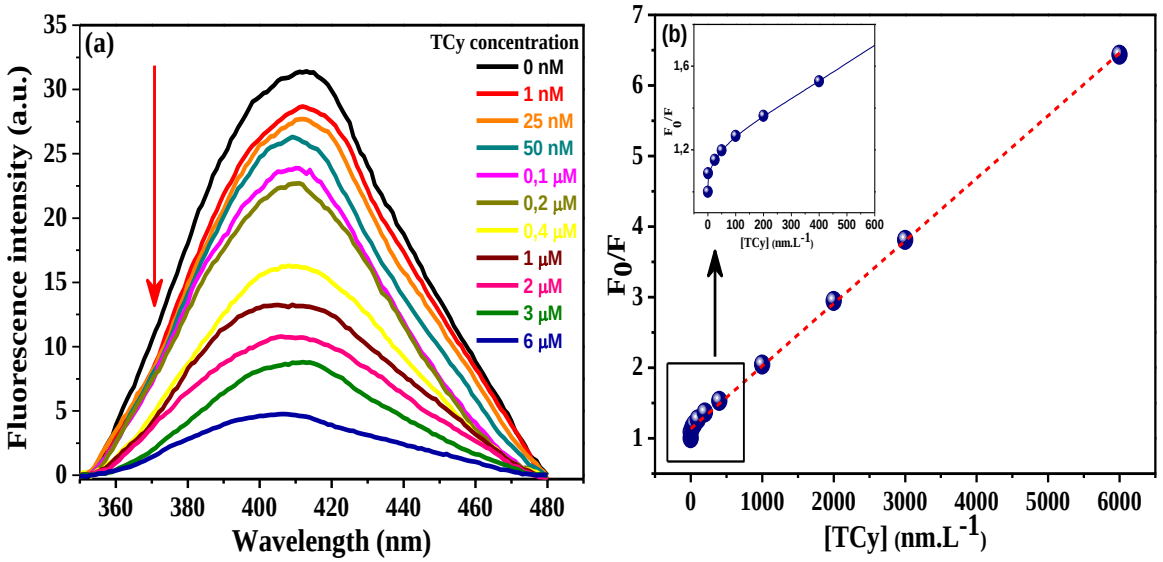

Fig. 11. Fluorescence spectra (λ_{exc} = 325 nm) of (a) TGA-ZnS QDs (0.2 mg mL^{-1}) in the presence of various concentrations of TCy (from top to bottom, 0, 25, 50, 100, 200, 400, 1000, 2000, 3000 and 6000 nM). (b) Linear fitted result using Stern–Volmer quenching plot of TCy concentration dependence on fluorescence intensity of TGA-ZnS QDs. Insert: zoom of Stern–Volmer plot at low concentration of TCy.

Owing to the very low LOD and the wide linear range of response, a high sensitivity is disclosed. The response of TGA-ZnS QDs might be due to two factors. Firstly, the carboxylate group has a high basicity. The consequence is a strong hydrogen bonding with the phenol and hydroxyl groups of TCy. Secondly, the TGA ligand has a short hydrocarbon chain between the thiol and the carboxylate groups, which can result in a highly ordered distribution on the surface of ZnS QDs, potentially increasing the hydrogen bonding interaction between TGA and TCy (**Fig. 12**).

Recently, there have been many reports on the detection methods of TCy listed in **Table 2**. Compared with these methods, our material is environment-friendly and the method is time-saving and an easy of operation and its works over a wide linear range. The afore mentioned findings show that the TGA-ZnS QDs can be used as suitable candidate for the detection of TCy, based on the lower detection limit and a wider detection range than previously reported methods.

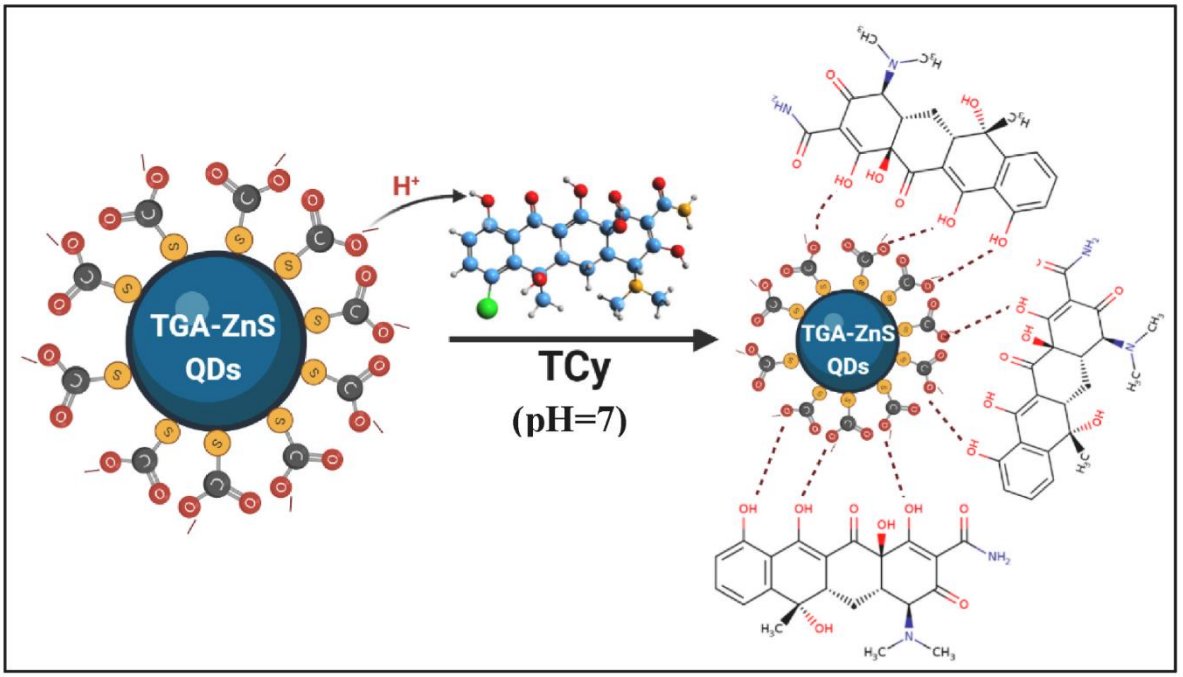

Fig. 12. Schematic representation of the electrostatic interaction between the positive charges of TCy and the negative charges of TGA-ZnS QDs.

Table 2. The linear range and detection limit of different assay methods for TCy

Method	Linear range (nM)	LOD (nM)	Reference
Adsorptive voltammetry carbon nanotube	100–2000	40	[51]
Ratiometric molecular imprinting	0–50	1.19	[52]
PEC detection ZrO_2/g-C_3N_4/FTO electrode	50–150	8.7	[53]
(TAP)/γ-cyclodextrin triple-helix aptamer probe/cyclodextrin fluorescent sensing	5–100	1.6	[54]
Carbon-doped WO_3 electrochemical aptasensor	0.1–100	0.048	[55]
Thioglycolic acid-ZnS QDs fluorescence probe	25–6000	0.03	This work

3.3.5. Analysis of tetracycline in biological samples

To investigate the applicability of the proposed method, our fluorescent probe was adapted to detect TCy in real samples (raw and pasteurized milk). Five spiked levels of TCy were added to the raw and pasteurized milk samples. As shown in **Fig. 13**, there is a linear relationship between the fluorescent intensity of TGA-ZnS QDs and the concentration of TCy in the range of 50 nM–3000 nM. The lowest detectable concentration of TCy in raw and pasteurized milk is 4.3 nM and 5.1 nM, respectively. As shown in **Table 3**, the excellent results (recoveries ranging from 98.4% to 100.8% and RSD values less than 0.6) confirm that the application of the proposed fluorescent probe in biological sample analysis was anticipated to be promising.

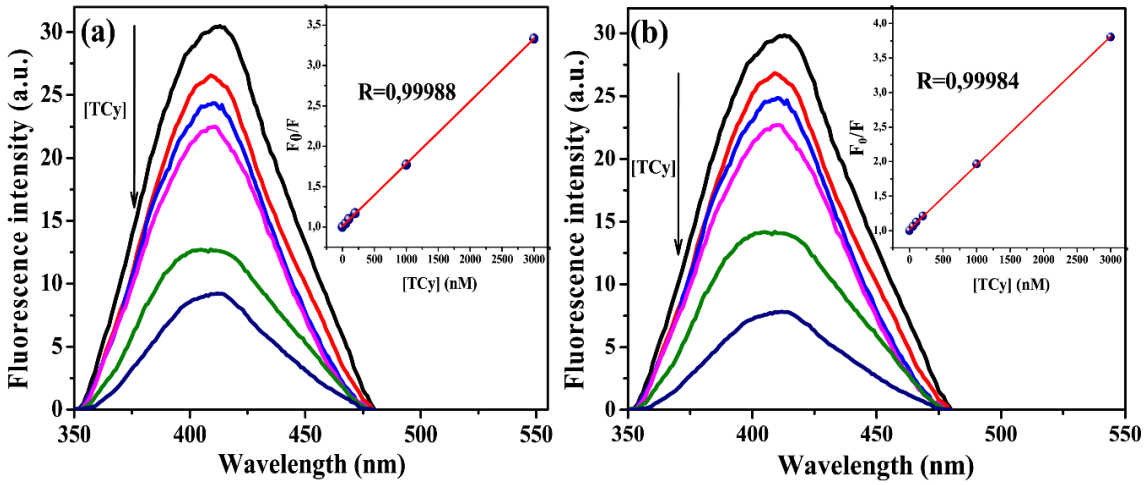

Fig. 13. Fluorescence spectra of TGA-ZnS QDs in (a) raw and (b) pasteurized milk samples containing 0, 50, 100, 200, 1000 and 3000 nM TCy. The inset is the linear relationship between the fluorescent intensity of TGA-ZnS and the concentrations of TCy in milk samples.

Table 3. Results for the determination of TCy in raw and pasteurized milk samples.

Samples	Added (nM)	Found[a] (nM) ± RSD (n = 3)	Recovery (%)
Raw milk	50	49.9 ± 0.4	99.8
	100	100.3 ± 0.3	100.3
	200	201.4 ± 0.4	100.7
	1000	992.7 ± 0.5	99.2
	3000	3003 ± 0.4	100.1
Pasteurized milk	50	50.2 ± 0.5	100.4
	100	98.4 ± 0.6	98.4
	200	201.7 ± 0.5	100.8
	1000	1001.6 ± 0.5	100.1
	3000	2998.1 ± 0.3	99.3

[a] Average of three replicate measurements ± relative standard deviation.

4. Conclusion

A simple, low cost, efficient and eco-friendly fluorescence sensor for the detection of trace TCy has been reported. The simple colloidal chemical approach employed for the synthesis of TGA-ZnS QDs provides a colloidal material with an excellent purity, low cost, easy implementation, and low energy consumption. Detection of TCy is based on the fluorescence quenching of TGA-ZnS QDs, is due to the electrostatic and hydrogen bonding interactions between the surface groups of ZnS QDs and TCy. Meanwhile, the TGA-ZnS QDs probe can be used for the detection of tetracycline in the range of 25–6000 nM with the LODs of 0.03 nM. In comparison to earlier published fluorescent sensors, the simple and low-cost TGA-ZnS QD fluorescence sensor reaches a very low limit of detection at the picomolar level. Besides, the sensor was successfully applied to TCy analysis in biological samples. It is believed that this research work has opened another avenue for the point of care detection of antibiotics in the biological fluids.

References

[1] C. Zhang *et al.*, Efficacy of carbonaceous nanocomposites for sorbing ionizable antibiotic sulfamethazine from aqueous solution, *Water Res.* 2016, 95, 103–112, doi: 10.1016/j.watres.2016.03.014.

[2] H. Yi *et al.*, Selective prepared carbon nanomaterials for advanced photocatalytic application in environmental pollutant treatment and hydrogen production, *Appl. Catal. B Environ.* 2018, 239, 408–424, doi: 10.1016/j.apcatb.2018.07.068.

[3] D. Huang *et al.*, Sorptive removal of ionizable antibiotic sulfamethazine from aqueous solution by graphene oxide-coated biochar nanocomposites: Influencing factors and mechanism, *Chemosphere* 2017, 186, 414–421, doi: 10.1016/j.chemosphere.2017.07.154.

[4] Z. Li, M. Li, Z. Zhang, P. Li, Y. Zang, X. Liu, Antibiotics in aquatic environments of China: A review and meta-analysis, *Ecotoxicol. Environ. Saf.* 2020, 199, 110668, doi: 10.1016/j.ecoenv.2020.110668.

[5] D. Fuoco, Classification framework and chemical biology of Tetracycline-structure-based drugs, *Antibiotics* 2012, 1, 1–13, doi: 10.3390/antibiotics1010001.

[6] S. Wang, W. Yong, J. Liu, L. Zhang, Q. Chen, Y. Dong, Development of an indirect competitive assay-based aptasensor for highly sensitive detection of tetracycline residue in honey, *Biosens. Bioelectron.* 2014, 57, 192–198, doi: 10.1016/j.bios.2014.02.032.

[7] F. Conzuelo, M. Gamella, S. Campuzano, A.J. Reviejo, J.M. Pingarrón, Disposable amperometric magneto-immunosensor for direct detection of tetracyclines antibiotics residues in milk, *Anal. Chim. Acta* 2012, 737, 29–36, doi: 10.1016/j.aca.2012.05.051.

[8] S. Wang, Y. Dong, X. Liang, Development of a SPR aptasensor containing oriented aptamer for direct capture and detection of tetracycline in multiple honey samples, *Biosens. Bioelectron.* 2018, 109, 1–7, doi: 10.1016/j.bios.2018.02.051.

[9] Y. Chen *et al.*, Near-infrared fluorescence-based multiplex lateral flow immunoassay for the simultaneous detection of four antibiotic residue families in milk, *Biosens. Bioelectron.* 2016, 79, 430–434, doi: 10.1016/j.bios.2015.12.062.

[10] J. Chen, S. Chen, F. Li, Instrument-free visual detection of tetracycline on an autocatalytic DNA machine using a caged G-quadruplex as the signal reporter, *Chem. Commun.* 2017, 53, 8743–8746, doi: 10.1039/c7cc04083k.

[11] J. Xu *et al.*, A novel visual ratiometric fluorescent sensing platform for highly- sensitive visual detection of tetracyclines by a lanthanide- functionalized palygorskite nanomaterial, *J. Hazard. Mater.* 2018, 342, 158–165, doi: 10.1016/j.jhazmat.2017.08.020.

[12] Z. Liu *et al.*, A novel fluorescence probe for rapid and sensitive detection of tetracyclines residues based on silicon quantum dots, *Spectrochim. Acta - Part A Mol. Biomol. Spectrosc.* 2020, 240, 118463, doi: 10.1016/j.saa.2020.118463.

[13] E. Lewis, O. Chamel, M. Mohsenin, E. Ots, E.T. White, Regulation (EC) No 1907/2006 of the European parliament and the council of 18 December 2006, *Off. J. Eur. Union I*, pp. 219–219, 2006, doi: 10.4324/9781315270326-156.

[14] X. Liu *et al.*, Recent advances in sensors for tetracycline antibiotics and their applications, *TrAC - Trends Anal. Chem.* 2018, 109, 260–274, doi: 10.1016/j.trac.2018.10.011.

[15] Q. Zhou, Y. Zhang, N. Wang, L. Zhu, H. Tang, Analysis of tetracyclines in chicken tissues and dung using LC-MS coupled with ultrasound-assisted enzymatic hydrolysis, *Food Control* 2014, 46, 324–331, doi: 10.1016/j.foodcont.2014.05.015.

[16] P. Moudgil, J.S. Bedi, R.S. Aulakh, J.P.S. Gill, A. Kumar, Validation of HPLC Multi-residue Method for Determination of Fluoroquinolones, Tetracycline, Sulphonamides and Chloramphenicol Residues in Bovine Milk, *Food Anal. Methods* 2019, 12, 338–346, doi: 10.1007/s12161-018-1365-0.

[17] W. Naidong, S. Hua, E. Roets, J. Hoogmartens, Assay and purity control of tetracycline, chlortetracycline and oxytetracycline in animal feeds and premixes by TLC densitometry with fluorescence detection, *J. Pharm. Biomed. Anal.* 2003, 33, 85–93, doi: 10.1016/S0731-7085(03)00153-5.

[18] I.S. Ibarra, J.A. Rodriguez, J.M. Miranda, M. Vega, E. Barrado, Magnetic solid phase extraction based on phenyl silica adsorbent for the determination of tetracyclines in milk samples by capillary electrophoresis, *J. Chromatogr. A* 2011, 1218, 2196–2202, doi: 10.1016/j.chroma.2011.02.046.

[19] J. Tong, Q. Rao, K. Zhu, Z. Jiang, S. Ding, Simultaneous determination of five tetracycline and macrolide

antibiotics in feeds using HPCE, *J. Sep. Sci.* 2009, 32, 4254–4260, doi: 10.1002/jssc.200900415.
[20] E. Song *et al.*, Multi-color quantum dot-based fluorescence immunoassay array for simultaneous visual detection of multiple antibiotic residues in milk, *Biosens. Bioelectron.* 2015, 72, 320–325, doi: 10.1016/j.bios.2015.05.018.
[21] P. Sharma, M.S. Mehata, Rapid sensing of lead metal ions in an aqueous medium by MoS_2 quantum dots fluorescence turn-off, *Mater. Res. Bull.* 2020, 131, 110978, doi: 10.1016/j.materresbull.2020.110978.
[22] L. Zhang, J. Wang, J. Deng, S. Wang, A novel fluorescent 'turn-on' aptasensor based on nitrogen-doped graphene quantum dots and hexagonal cobalt oxyhydroxide nanoflakes to detect tetracycline, *Anal. Bioanal. Chem.* 2020, 412, 1343–1351, doi: 10.1007/s00216-019-02361-5.
[23] V. Sharma, M.S. Mehata, Rapid optical sensor for recognition of explosive 2,4,6-TNP traces in water through fluorescent ZnSe quantum dots, *Spectrochim. Acta - Part A Mol. Biomol. Spectrosc.* 2021, 260, 119937, doi: 10.1016/j.saa.2021.119937.
[24] M. Ramezani, N.M. Danesh, P. Lavaee, K. Abnous, S.M. Taghdisi, A novel colorimetric triple-helix molecular switch aptasensor for ultrasensitive detection of tetracycline, *Biosens. Bioelectron.* 2015, 70, 181–187, doi: 10.1016/j.bios.2015.03.040.
[25] Y. Wang *et al.*, A colorimetric biosensor using Fe_3O_4 nanoparticles for highly sensitive and selective detection of tetracyclines, *Sensors Actuators, B Chem.* 2016, 236, 621–626, doi: 10.1016/j.snb.2016.06.029.
[26] Y. Feng, D. Zhong, H. Miao, X. Yang, Carbon dots derived from rose flowers for tetracycline sensing, *Talanta*, 2015, 140, 128–133, doi: 10.1016/j.talanta.2015.03.038.
[27] V. Sharma, M.S. Mehata, Synthesis of photoactivated highly fluorescent Mn^{2+}- doped ZnSe quantum dots as effective lead sensor in drinking water, *Mater. Res. Bull.* 2021, 134, 111121, doi: 10.1016/j.materresbull.2020.111121.
[28] N. Ben Brahim *et al.*, Interaction of l-cysteine functionalized CdSe quantum dots with metallic cations and selective binding of cobalt in water probed by fluorescence, *Sensors Actuators B Chem.* 2017, 243, 489–499, doi: 10.1016/j.snb.2016.12.003.
[29] Y. Zhang *et al.*, The synthesis of high bright silver nanoclusters with aggregation- induced emission for detection of tetracycline, *Sensors Actuators, B Chem.* 2021, 326, 129009, doi: 10.1016/j.snb.2020.129009.
[30] J. Guo *et al.*, Copper doped carbon dots as the multi-functional fluorescent sensing platform for tetracyclines and pH, *Sensors Actuators B Chem.* 2021, 330, 129360, doi: 10.1016/j.snb.2020.129360.
[31] T.P. Nguyen, Q.V. Lam, T.B. Vu, Energy transfer in poly(vinyl alcohol)-encapsulated Mn-doped ZnS quantum dots, *J. Lumin.* 2018, 203, 533–539, doi: 10.1016/j.jlumin.2018.07.010.
[32] D. Li, J. Qin, Q. Xu, G. Yan, A room-temperature phosphorescence sensor for the detection of alkaline phosphatase activity based on Mn-doped ZnS quantum dots, *Sensors Actuators B Chem.* 2018, 274, 78–84, doi: 10.1016/j.snb.2018.07.108.
[33] K. Mili, Z. Hsine, Y. Chevalier, S. Hbaieb, R. Mlika, ZnS quantum dots as fluorescence sensor for quantitative detection of tetracycline, *Opt. Mater. (Amsterdam).* 2022, 125, 112103, doi: 10.1016/j.optmat.2022.112103.
[34] F. Dehghan, M. Molaei, F. Amirian, M. Karimipour, A.R. Bahador, Improvement of the optical and photocatalytic properties of ZnSe QDs by growth of ZnS shell using a new approach, *Mater. Chem. Phys.* 2018, 206, 76–84, doi: 10.1016/j. matchemphys.2017.11.061.
[35] Z. Pourghobadi, H. Makanali, H. Zare, Highly sensitive fluorescent probe for detection of paraquat based on nanocrystals, *J. Fluoresc.* 2021, 31, 559–567, doi: 10.1007/s10895-020-02679-9.
[36] S. Ouni, N. Bel Haj Mohamed, M. Bouzidi, A. Bonilla-Petriciolet, M. Haouari, High impact of thiol capped ZnS nanocrystals on the degradation of single and binary aqueous solutions of industrial azo dyes under sunlight, *J. Environ. Chem. Eng.* 2021, 9, 105915, doi: 10.1016/j.jece.2021.105915.
[37] D.A. Reddy, C. Liu, R.P. Vijayalakshmi, B. K. Reddy, Effect of Al doping on the structural, optical and photoluminescence properties of ZnS nanoparticles, *J. Alloys Compd.* 2014, 582, 257–264, doi: 10.1016/j.jallcom.2013.08.051.
[38] L. Li, Y. Cheng, Y. Ding, Y. Lu, F. Zhang, Application of thioglycolic acid capped nano-ZnS as a fluorescence probe for the determination of nevirapine, *Anal. Methods* 2012, 4, 4213–4219, doi: 10.1039/c2ay26002f.
[39] R. Khafajeh, M. Molaei, M. Karimipour, Synthesis of ZnSe and ZnSe:Cu quantum dots by a room temperature photochemical (UV-assisted) approach using Na_2SeO_3 as Se source and investigating optical properties, *Luminescence* 2017, 32, 581–587, doi: 10.1002/bio.3224.
[40] F. Amirian, M. Molaei, M. Karimipour, A.R. Bahador, A new and simple UV- assisted approach for synthesis

of water soluble ZnS and transition metals doped ZnS nanoparticles (NPs) and investigating optical and photocatalyst properties, *J. Lumin.* 2018, 196, 174–180, doi: 10.1016/j.jlumin.2017.12.005.

[41] T.S. Tilakraj, M.K. Patil, V.S. Bhat, V. Pujari, S.R. Inamdar, Simple one pot synthesis and characterization of biocompatible Lactic acid capped fluorescent ZnS QDs, *Mater. Today Proc.* 2021, 47, 4189–4193, doi: 10.1016/j.matpr.2021.04.455.

[42] M. Dhanam, B. Kavitha, S. Velumani, An investigation on silar $Cu(In_{1-x}Al_x)Se_2$ thin films, *Mater. Sci. Eng. B Solid-State Mater. Adv. Technol.* 2010, 174, 209–215, doi: 10.1016/j.mseb.2010.03.028.

[43] M. Dhanam, B. Kavitha, N. Jose, D.P. Devasia, Analysis of ZnS nanoparticles prepared by surfactant micelle-template inducing reaction, *Chalcogenide Lett.* 2009, 6, 713–722.

[44] Y. Wang *et al.*, Simple and greener synthesis of highly photoluminescence Mn^{2+} - doped ZnS quantum dots and its surface passivation mechanism, *Appl. Surf. Sci.* 2014, 316, 54–61, doi: 10.1016/j.apsusc.2014.07.135.

[45] R. Subha *et al.*, Efficient photoluminescence of Mn^{2+}-doped ZnS quantum dots excited by two-photon absorption in near-infrared window II, *J. Phys. Chem. C* 2013, 117, 20905–20911, doi: 10.1021/jp404124c.

[46] H. Li, W. Y. Shih, W.H. Shih, Highly photoluminescent and stable aqueous ZnS quantum dots, *Ind. Eng. Chem. Res.* 2010, 49, 578–582, doi: 10.1021/ie901086d.

[47] J. Tauc, Optical properties and electronic structure of amorphous Ge and Si, *BMC Public Health* 1968, 5, 1–8, doi: 10.1016/0025-5408(68)90023-8.

[48] N. Ben Brahim *et al.*, Synthesis, characterization and spectral temperature-dependenceof thioglycerol-CdSe nanocrystals, *J. Lumin.* 2016, 177, 402–408, doi: 10.1016/j.jlumin.2016.05.026.

[49] R.N. Juine, A. Das, Surfactant-Free Green Synthesis of ZnS QDs with Active Surface Defects for Selective Nanomolar Oxalic Acid Colorimetric Sensors at Room Temperature, *ACS Sustain. Chem. Eng.* 2020, 8, 11579–11587, doi: 10.1021/acssuschemeng.0c02784.

[50] S. Prasanth, P. Irshad, D.R. Raj, T.V. Vineeshkumar, R. Philip, C. Sudarsanakumar, Nonlinear optical property and fluorescence quenching behavior of PVP capped ZnS nanoparticles co-doped with Mn^{2+} and Sm^{3+}, *J. Lumin.* 2015, 166, 167–175, doi: 10.1016/j.jlumin.2015.05.028.

[51] B. Bahmani, F. Moztarzadeh, M. Rabiee, Synthesis of zinc sulfide semiconductor nanoparticles by coprecipitation method for biological diagnostics, *J. Optoelectron. Adv. Mater.* 2007, 9, 3336–3339.

[52] P. Sana, L. Hashmi, M. M. Malik, Luminescence and Morphological Kinetics of Functionalized ZnS Colloidal Nanocrystals, *ISRN Opt.*, 2012, 2012, 1–8, doi: 10.5402/2012/621908.

[53] M.T. Reetz, W. Helbig, Size-Selective Synthesis of Nanostructured Transition Metal Clusters, *J. Am. Chem. Soc.* 1994, 116, 7401–7402, doi: 10.1021/ja00095a051.

[54] J. Cizeron, M.P. Pileni, Solid solution of $Cd_yZn_{1-y}S$ nanosize particles made in reverse micelles, *J. Phys. Chem.* 1995, 99, 17410–17416, doi: 10.1021/j100048a016.

[55] N. Bansal, G.C. Mohanta, K. Singh, Effect of Mn^{2+} and Cu^{2+} co-doping on structural and luminescent properties of ZnS nanoparticles, *Ceram. Int.* 2017, 43, 7193–7201, doi: 10.1016/j.ceramint.2017.03.007.

[56] H. Zhou *et al.*, Understanding the mechanoluminescent mechanisms of manganese doped zinc sulfide based on load effects, *J. Lumin.* 2018, 203, 683–688, doi: 10.1016/j.jlumin.2018.07.018.

[57] S. Ebrahimi, B. Yarmand, N. Naderi, Enhanced optoelectrical properties of Mn- doped ZnS films deposited by spray pyrolysis for ultraviolet detection applications, *Thin Solid Films* 2019, 676, 31–41, doi: 10.1016/j.tsf.2019.02.046.

[58] P. Sakthivel, S. Muthukumaran, M. Ashokkumar, Structural, band gap and photoluminescence behaviour of Mn-doped ZnS quantum dots annealed under Ar atmosphere, *J. Mater. Sci. Mater. Electron.* 2015, 26, 1533–1542, doi: 10.1007/s10854-014-2572-0.

[59] S.R. Chalana, V.S. Kavitha, R. Reshmi Krishnan, V.P. Mahadevan Pillai, Tailoring the visible emissions in ZnS:Mn films for white light generation, *J. Alloys Compd.* 2019, 771, 721–735, doi: 10.1016/j.jallcom.2018.08.275.

[60] S.K. Panda, S. Chaudhuri, Chelating ligand-mediated synthesis of hollow ZnS microspheres and its optical properties, *J. Colloid Interface Sci.* 2007, 313, 338–344, doi: 10.1016/j.jcis.2007.04.032.

[61] C.S. Pathak, D.D. Mishra, V. Agarwala, M.K. Mandal, Blue light emission from barium doped zinc sulfide nanoparticles, *Ceram. Int.* 2012, 38, 5497–5500, doi: 10.1016/j.ceramint.2012.03.063.

[62] C. Bi *et al.*, Synthesis and characterization of Co-doped wurtzite ZnS nanocrystals, *Mater. Chem. Phys.* 2009, 116, 363–367, doi: 10.1016/j.matchemphys.2009.03.037.

[63] N.T. Hien *et al.*, Structural, optical properties, energy transfer mechanism and quantum cutting of Tb^{3+} doped

ZnS quantum dots, *J. Phys. Chem. Solids* 2020, 147, 109638, doi: 10.1016/j.jpcs.2020.109638.
[64] M. Hafeez *et al.*, Critical role of defect states on visible luminescence from ZnS nanostructures doped with Au, Mn and Ga, *Mater. Sci. Semicond. Process.* 2020, 117, 105193, doi: 10.1016/j.mssp.2020.105193.
[65] X. Wang, J. Shi, Z. Feng, M. Li, C. Li, Visible emission characteristics from different defects of ZnS nanocrystals, *Phys. Chem. Chem. Phys.*, 2011, 13, 4715–4723, doi: 10.1039/c0cp01620a.
[66] S.F. Wuister, C. De Mello Donegá, A. Meijerink, Luminescence temperature antiquenching of water-soluble CdTe quantum dots: Role of the solvent, *J. Am. Chem. Soc.* 2004, 126, 10397–10402, doi: 10.1021/ja048222a.
[67] Y. Nonoguchi, T. Nakashima, T. Kawai, Size- and temperature-dependent emission properties of zinc-blende CdTe nanocrystals in ionic liquid, *J. Phys. Chem. C* 2007, 111, 11811–11815, doi: 10.1021/jp073152q.
[68] D. Denzler, M. Olschewski, K. Sattler, Luminescence studies of localized gap states in colloidal ZnS nanocrystals, *J. Appl. Phys.* 1998, 84, 2841–2845, doi: 10.1063/1.368425.
[69] N. Bel Haj Mohamed, N. Ben Brahim, R. Mrad, M. Haouari, R. Ben Chaâbane, M. Negrerie, Use of MPA-capped CdS quantum dots for sensitive detection and quantification of Co^{2+} ions in aqueous solution, *Anal. Chim. Acta* 2018, 1028, 50–58, doi: 10.1016/j.aca.2018.04.041.
[70] D.E. Ramírez-Herrera *et al.*, NIR-emitting alloyed CdTeSe QDs and organic dye assemblies: A nontoxic, stable, and efficient FRET system, *Nanomaterials* 2018, 8, 231, doi: 10.3390/nano8040231.
[71] S. Chen *et al.*, CdSe quantum dots decorated by mercaptosuccinic acid as fluorescence probe for Cu^{2+}, *J. Lumin.* 2011, 131, 947–951, doi: 10.1016/j.jlumin.2010.12.029.
[72] W.E. Mahmoud, Functionalized ME-capped CdSe quantum dots based luminescence probe for detection of Ba^{2+} ions, *Sensors Actuators B Chem.* 2012, 164, 76–81, doi: 10.1016/j.snb.2012.01.073.
[73] X. Cao *et al.*, Facile synthesis of chitosan-capped ZnS quantum dots as an eco-friendly fluorescence sensor for rapid determination of bisphenol A in water and plastic samples, *RSC Adv.* 2014, 4, 16597–16606, doi: 10.1039/c3ra47868h.
[74] J. Duan, X. Jiang, S. Ni, M. Yang, J. Zhan, Facile synthesis of N-acetyl-l-cysteine capped ZnS quantum dots as an eco-friendly fluorescence sensor for Hg^{2+}, *Talanta* 2011, 85, 1738–1743, doi: 10.1016/j.talanta.2011.06.071.
[75] S. Mandani, B. Rezaei, A.A. Ensafi, M.R. Sabzalian, Development of a new simple spectroscopic determination coupled acid-motivated delivery system based on fluorescence turn-off MSNs@MPA-ZnS QDs for infection, *Microporous Mesoporous Mater.* 2021, 317, 110971, doi: 10.1016/j.micromeso.2021.110971.
[76] L. Zhang, L. Chen, Fluorescence Probe Based on Hybrid Mesoporous Silica/Quantum Dot/Molecularly Imprinted Polymer for Detection of Tetracycline, *ACS Appl. Mater. Interfaces* 2016, 8, 16248–16256, doi: 10.1021/acsami.6b04381.
[77] H. Shao *et al.*, An ion-imprinted material embedded carbon quantum dots for selective fluorometric determination of lithium ion in water samples, *Microchim. Acta* 2017, 184, 4861–4868, doi: 10.1007/s00604-017-2493-8.